scientific reports

Check for updates

OPEN

Synergistic bactericidal and anticancer potential of rubidium and silver-containing phosphate-based bioglasses

M. Bosca[1], L. C. Bolundut[1], L. Pop[1], R. Lucacel-Ciceo[2,3]✉, G. Stiufiuc[2], R. F. Badila[2], I. Lupan[3,4], O. R. Koblicska[3], A. Onaciu[5], D. Cenariu[5], A.-B. Țigu[5], G. Katona[6], D. Simedru[7] & P. Pascuta[1]✉

A new vitreous system, $44P_2O_5{\cdot}25CaO{\cdot}21Na_2O{\cdot}5ZnO{\cdot}5Ag_2O$, doped with 1–7 mol% Rb_2O, was synthesized by conventional melt quenching, and the structural and biological effects of rubidium incorporation were systematically investigated. The X-ray diffraction confirmed the amorphous nature of all compositions, while FTIR and Raman spectroscopy revealed that Rb^+ ions act as network modifiers, promoting progressive depolymerization of the phosphate network dominated by Q^2 and Q^1 units. X-ray photoelectron spectroscopy demonstrated the presence of all constituent elements at the glass surface, with silver detected in both ionic (Ag^+) and metallic (Ag^0) states; the Ag^+/Ag^0 ratio varied slightly (0.62–0.65) with Rb_2O addition, indicating stable coexistence of ionic species and metallic nanoparticle clusters. Transmission electron microscopy corroborated the formation of Ag-containing nanoclusters dispersed within the vitreous matrix. Biological performance was evaluated through a comprehensive series of assays, including fibroblast viability (MTT), antimicrobial, antifungal, and anticancer tests. Human skin fibroblasts displayed a high proliferation rate at both 24 and 48 h, confirming the excellent cytocompatibility of the glass system in the 0–5 mol% Rb_2O compositional range. In contrast, a pronounced cytotoxic effect was recorded against breast cancer cells for the composition containing 7 mol% Rb_2O at a concentration of 0.78 mg mL^{-1} after 48 h. Antimicrobial testing revealed complete elimination of gram-negative bacteria within 1 h, attributed primarily to Ag^+ release. A bacteriostatic effect against gram-positive strains at 2 h, as well as inhibition of fungal propagation at 4 h, was also observed and correlated with the surface concentration of silver and rubidium.

Keywords Phosphate glasses, Rb_2O, Ag_2O, Cell viability, Antibacterial activity

Phosphate based bio-glasses (BGs) having calcium (Ca), sodium (Na) and/or potassium (K) are one of the basic compositions designed for applications in hard/soft tissue engineering, drug delivery, therapeutic ion release and as coatings on metallic implants for orthopedics and dentistry[1–5]. Throughout time, calcium phosphate-based BGs have evolved from implantable inert substances to bioactive materials. Notably, they have become integral components of bioresorbable photonic devices, highlighting their adaptability and vast potential within biomedical applications[6,7].

The expanding demands of medicine and engineering have driven the development of new compositions and tailored synthesis methods to meet specific functional requirements. To achieve enhancement for the biological performance of these vitreous materials, almost all periodic table elements of the have been investigated for incorporation into BG formulations. Studies have demonstrated that the inclusion of metallic, non-metallic,

[1]Faculty of Materials and Environmental Engineering, Technical University of Cluj-Napoca, Cluj-Napoca 400641, Romania. [2]Faculty of Physics, Babes-Bolyai University, Cluj-Napoca 400084, Romania. [3]Institute for Interdisciplinary Research in Bio-Nano-Sciences, Babes-Bolyai University, Cluj-Napoca 400271, Romania. [4]Faculty of Biology and Geology, Babes-Bolyai University, Cluj- Napoca 400084, Romania. [5]Institute of Medical Research and Life Sciences – MEDFUTURE, Cluj-Napoca 400349, Romania. [6]Faculty of Chemistry and Chemical Engineering, Babes-Bolyai University, Cluj-Napoca 400028, Romania. [7]Subsidiary Research Institute for Analytical Instrumentation, INCDO-INOE 2000, Cluj-Napoca 400293, Romania. ✉email: raluca.lucacel@ubbcluj.ro; Petru.Pascuta@phys.utcluj.ro

and rare-earth biologically active ions can significantly influence the osteogenic, angiogenic, anti-inflammatory, anti-tumoral, and antibacterial properties of BGs[8,9].

Infection remains a significant challenge in implantology, where primary contributors to implant failure are bacterial adhesion and biofilm formation[10–12]. Killing the bacteria within the immediate vicinity of the implant is crucial but difficult since the delivery of antibiotics to the infected area is relates with the poor vascularization in the bone tissue. Moreover, antibiotic resistance occurs frequently and usually within a few days of treatment initiation (e.g., with frequency 3×10^{-6} for fusacid)[13].

Zinc, is one of the most important trace elements in the human body, is often present in the composition of biomaterials since it is associated with the growth and development of healthy bone[14,15]. Zinc is also a key factor in many enzymes and supports protein combinations and it is essential for DNA replication. In addition to its biological roles, Zn^{2+} ions incorporated into bioactive glasses (BGs) have been shown to exhibit significant antibacterial and anti-inflammatory effects[8,16–18]. These properties make zinc a valuable addition to BG formulations, enhancing their therapeutic potential by promoting healing while preventing infections.

Among the less common elements, rubidium (Rb), an alkali element from the Group 1 of the Periodic Table has garnered attention for its diverse applications across various technological areas, including energy, medicine, catalysis, ferromagnetic materials, solders, and specialty glasses[19]. Rubidium is characterized by low toxicity and can be found in several human organs, such as the heart, pancreas, cerebrum, liver and kidneys, where it functions similarly to potassium, playing an essential role in cellular processes[19,20]. The application of rubidium doped silica-based biomaterials has been focused on bond reconstruction revealing the capability of Rb ions to promote the angiogenesis and osteogenesis[21,22]. Furthermore, rubidium-containing BGs have been reported to exhibit antibacterial and anticancer properties, highlighting their potential for wound healing and cancer treatment applications[23,24]. In terms of structural role within the glass network, rubidium behaves similarly to other alkali metals. It disrupts the glass network structure by breaking the glass former chains and creating non-bridging oxygen atoms (NBOs).

Silver ions (Ag^{+}) have long been recognized for their potent antibacterial properties, a characteristic that dates to antiquity, and they remain one of the most widely utilized elements in BGs for antimicrobial applications[25,26]. However, the successful incorporation of silver into BGs presents challenges, particularly in ensuring that the silver is present in its ionic form. The metallic form of silver does not exhibit significant bacteriostatic or bactericidal effects[27–30]. Therefore, the method of synthesis plays a key role in achieving the desired ionic form of silver in the glass matrix. The sol-gel method has been proven to be more effective in incorporating ionic silver into BGs compared to traditional melt-quenching processes, facilitating better control over silver's oxidation state and distribution[31]. Recent studies have also explored the synergistic effect of zinc (Zn^{2+}) and silver (Ag^{+}) ions in sol-gel derived BGs, focusing on understanding the relationship between the structural properties of these materials and their biological behaviour to find new applications of this class of materials[8,32]. Beyond the oxidation state of silver, the size of silver particles plays a crucial role in biomedical applications. Silver nanoparticles (Ag NPs) exhibit significant potential across a wide range of applications, including antimicrobial agents, biomedical device coatings, drug delivery systems, imaging probes, and diagnostic and optoelectronic platforms. Their unique physical and optical properties, as well as their biochemical functionality, can be precisely tailored through controlling its size and shape[33].

Despite the extensive study of phosphate-based bioglasses (BGs), the incorporation of rubidium ions into these systems, particularly those synthesized via the melt-quenching method, remains unexplored. This study aims to develop and characterize a novel class of rubidium-containing BGs with the composition $xRb_2O\cdot(100\text{-}x)[44P_2O_5\cdot25CaO\cdot21Na_2O\cdot5ZnO\cdot5Ag_2O]$. The research focuses on investigating their structural, physicochemical, and biological properties, emphasizing biocompatibility, anticancer activity, bactericidal efficacy, and antifungal potential. By leveraging the synergistic interaction between silver and rubidium ions, this study seeks to enhance the biological functionality of the glasses, with promising implications for biomedical applications such as bone regeneration, infection control, and targeted cancer therapy.

Experimental procedure

Materials

Reagents of high purity Rb_2CO_3, $NH_4H_2PO_4$, CaO, $Na_2CO_3\cdot10H_2O$, ZnO and Ag_2O were used in stoichiometric amounts to obtain samples from a new glass system that has the following chemical compositions $xRb_2O\cdot(100\text{-}x)[44P_2O_5\cdot25CaO\cdot21Na_2O\cdot5ZnO\cdot5Ag_2O]$, with $0 \le x \le 7$ mol%. The samples were prepared by using the conventional melt quenching technique. The used oxides were mixed through grinding inside an agate mortar obtaining a homogeneous mixture. The highly homogenized mixtures of the corresponding reagents were placed in sintered corundum crucibles which were introduced for melting directly at 1250 °C in an electric furnace and were kept at this temperature for 15 min. The melt was then quickly cooled to room temperature by pouring onto stainless-steel plates.

Characterization

X-ray diffraction (XRD) data were recorded at the room temperature with a Shimadzu 6000 XRD diffractometer with Cu-K_α radiation ($\lambda = 1.54$ Å) having the source power of 40 kV and 30 mA.

The FTIR absorption spectra of the samples were recorded with a JASCO FTIR 6200 spectrometer, in the range 400–4000 cm^{-1}, at room temperature, spectral resolution of 4 cm^{-1}, using the KBr pellet technique.

The Raman spectra were recorded with a confocal Renishaw®inVia microscope (Renishaw plc, Wotton-under-Edge, Gloucestershire, UK), equipped with a Leica microscope (Leica Microsystems GmbH, Wetzlar, Germany), using a 50× objective (N.A. 0.75) and a 785 nm diode laser (Renishaw, Wotton-under-Edge, UK) for excitation. The calibration procedure was performed by using an internal silicon reference before measuring the samples. The laser power (measured at the sample surface) was ~113 mW and the acquisition time was set to

40 s (10 s integration time and 4 accumulations). The spectrograph was equipped with a 600 lines/mm grating and a charge coupled device camera (CCD). The spectral resolution of the spectrometer was ~2 cm^{-1}. The baseline correction was performed by using the Wire 4.2 software provided by Renishaw plc (Wotton-under-Edge, Gluocestershire, UK), with the inVia spectrometer.

The FTIR and Raman results were processed by using OriginPro 2019 software (OriginLab, Nothampton, Massachusetts, USA).

The X-ray photoelectron spectroscopy (XPS) analysis was conducted on finely powdered samples using a SPECS PHOIBOS 150 MCD system equipped with monochromatic Al Kα source (250 W, $h\nu = 1486.6$ eV), hemispherical analyser and multichannel detector. The typical vacuum in the analysis chamber during the measurements was in the range of 10^{-9}–10^{-10} mbar. Charge neutralization was used for all samples. The binding energy (BE) scale was charge referenced to the C1s photoelectron peak at 284.6 eV. The elemental composition on samples surface was calculated by a standard quantitative XPS analysis of survey spectra acquired at pass energy of 60 eV in the binding energy range 0–1200 eV. High-resolution spectra were obtained using analyser pass energy of 20 eV. The atomic concentrations were estimated from the areas of the characteristic photoelectron lines assuming a Shirley type background. For the analysis of high-resolution spectra all peaks were deconvoluted and fitted using Shirley background and GL(30) line shapes, i.e. a combination of Gaussian (70%) and Lorentzian (30%) line shapes. The position and full width at half maximum of photoelectron peaks were estimated by spectra deconvolution with Casa XPS (Casa Software Ltd., UK).

Transmission electron microscopy (TEM) images were acquired using a Hitachi H-7650 transmission electron microscope operating at an acceleration voltage of 80 keV. For sample preparation, approximately 1 mg of the material was suspended in 1 mL of CH_3OH with sonication to ensure dispersion. A drop of the resulting suspension was then placed onto a Formvar/Carbon-coated copper grid (300 mesh) and allowed to evaporate before imaging.

Cell culture and MTT test

In vitro studies were performed on two different cell lines: CCD1137Sk (human skin fibroblast, non-tumoral) and HS578T (triple negative breast cancer cells). They were grown in IMDM cell culture medium (for CCD1137Sk) and RPMI 1640 (for HS578T cells) both supplemented with 10% fetal bovine serum (FBS) and 1% L-glutamine. Cells were kept at 37 °C in a humidified chamber with 5% CO_2. All reagents used for cell growth were bought from Gibco (Grand Island, NY, USA). All the cells were bought from ATCC.

The cytotoxicity of the compounds was assessed using the MTT test. For this, 10,000 cells/well were cultivated in 96 well plates. The cells were allowed to adhere for 24 h after which treatments were added at different concentrations in the range of 0.78–100 mg/mL. The MTT assay was performed at 24 and 48 h by reading the absorbance at 570 nm with the help of the SPARK 10 M spectrophotometer (Tecan, Männedorf, Switzerland). The results were analyzed using Graphpad Prism 6 software and are presented as means ± standard error of the mean of four independent experiments.

Antibacterial and antifungal tests

The antibacterial activity of the samples was assessed on the Gram-positive bacterium *Staphylococcus aureus* (ATCC 1109R) and the Gram-negative bacterium *Escherichia coli* (ATCC 25922). A quantity of 30 mg of each sample was mixed with the bacterial suspension in liquid culture (10^4 cells/mL). Then, 25 µL of the culture was plated on solid medium (Mueller-Hinton agar) and incubated overnight at 37 °C (the cells were plated in triplicate). Negative control (NC) was performed in the same way but without the samples. The Colony Forming Units (CFU) were counted the following day.

Antifungal tests were performed using *Candida albicans* cells as described above for the antibacterial tests. The Mueller-Hinton medium was used for bacterial cultures, while the blood agar medium was used for *Candida* cultures.

Results and discussion

XRD data

The solubility of Ag_2O in glass melts is the key factor for the effective production of Ag-containing BGs since silver is known as an element difficult to insert homogeneously in a glass composition. The XRD patterns of the investigated materials (Fig. 1) are characterized by broad lines characteristic for vitreous structure.

No changes were seen in the shape of diffractograms upon the Rb_2O additions. These features show: *(i)* a good solubility of silver ions in the $44P_2O_5{\cdot}25CaO{\cdot}21Na_2O{\cdot}5ZnO{\cdot}5Ag_2O$ system and *(ii)* a stable vitreous structure of the synthesized samples. Using the relation $R = (5\lambda)/(8\sin\theta)$[34], the average distance between the atoms in the first coordination sphere was determined to be approximately 3.8 Å. This distance is still nearly constant across the entire concentration range of Rb_2O revealing the rigidity of the glass network.

FTIR and Raman data

The FTIR spectra between 400 and 2000 cm^{-1} on the studied glasses with different content of rubidium oxide were collected and illustrated in Fig. 2. The broadening of the IR bands suggests the presence of structural disorder in the glass network.

The main bands of the spectra occur in the range of 400–1500 cm^{-1} and are assigned to the phosphate linkages vibration[35–39]. It is well known that the phosphate glass network is made of corner-sharing PO_4 tetrahedral units with one, two, three or four non-bridging oxygen (NBO)[37]. According to their mutual connectivity, these units can be classified by Q^n terms, where n represents the number of bridging oxygen's (BO) per tetrahedron with values ranging from 0 to 3.

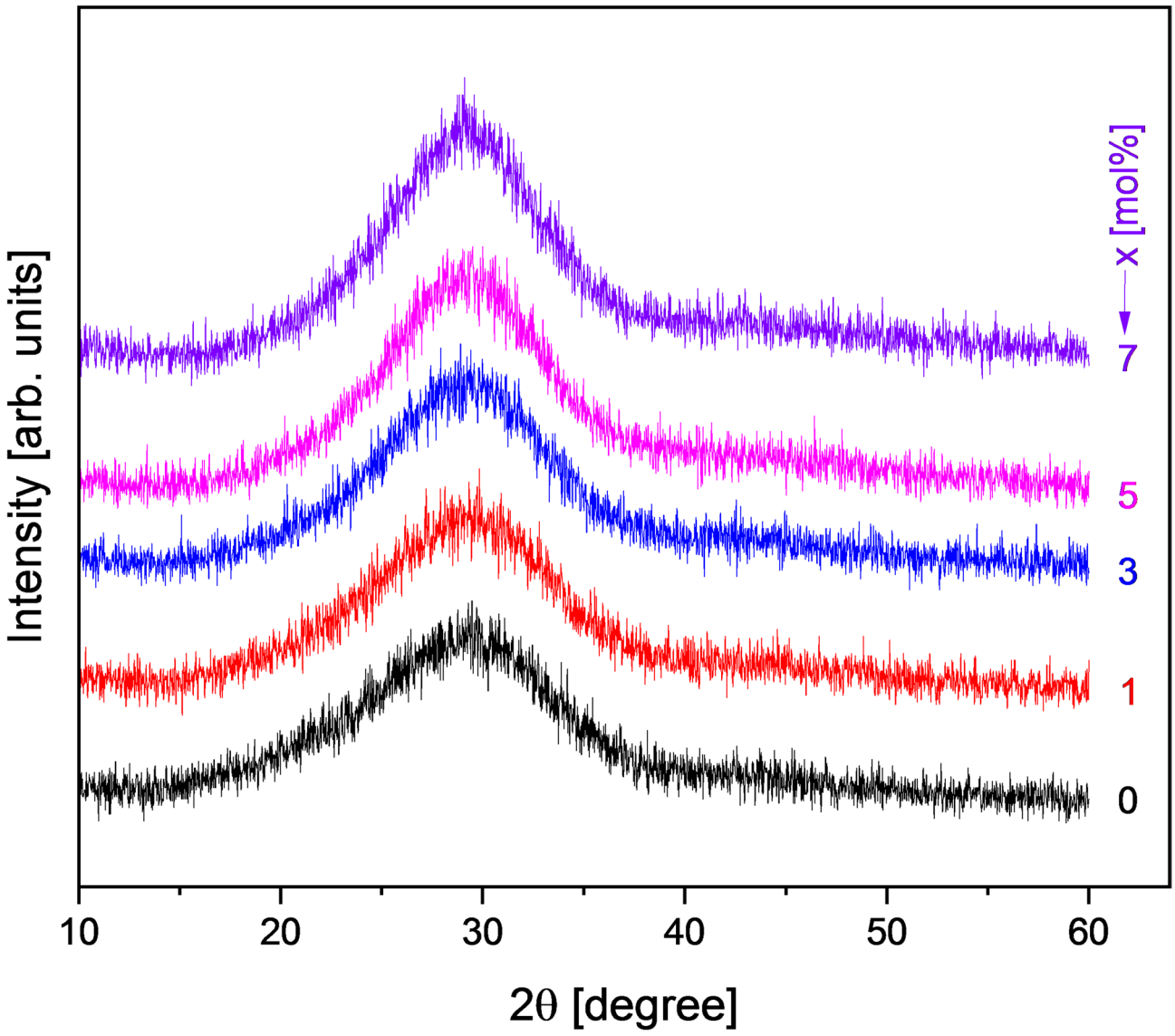

Fig. 1. XRD patterns of the $xRb_2O·(100-x)[44P_2O_5·25CaO·21Na_2O·5ZnO·5Ag_2O]$ glasses.

The absorption band observed around 545 cm^{-1} is attributed to the bending vibrations of O = P–O bonds, while the band appearing at approximately 430 cm^{-1} corresponds to P–O–M bonds, where M represents Ca, Na, Zn, or Rb[37,38,40]. Notably, the intensity of the 430 cm^{-1} band increases with higher Rb_2O content, indicating structural alterations in the glass matrix. This suggests that rubidium ions are incorporated into the phosphate network via non-bridging oxygen (NBO) atoms, thereby functioning as network modifiers.

The band centered around 745 cm^{-1} is associated with the symmetric stretching of bridging oxygen atoms bonded to phosphorus within Q^2 units[37–39]. Additionally, the asymmetric stretching band of P–O–P, initially positioned at approximately 900 cm^{-1}, shifts to ~ 915 cm^{-1} in correlation with increasing rubidium concentration. This shift, along with the increased intensity of the band, suggests that rubidium ions exert a polarization effect on the phosphate network, leading to structural modifications. These changes reflect the progressive depolymerization of longer phosphate chains into shorter segments and the subsequent formation of Q^1 pyrophosphate units[35].

Further structural insights are provided by the presence of absorption bands at approximately 990 cm^{-1} and 1115 cm^{-1}, corresponding to the symmetric and asymmetric stretching modes of chain-terminating Q^1 units, respectively[39]. The absorption band at ~ 1170 cm^{-1} is attributed to the symmetric stretching mode of O–P–O non-bridging oxygens, indicating the distribution of phosphate ions within Q^2 tetrahedra[35,37,39,41]. Moreover, the asymmetric stretching vibration of the P = O bond, characteristic of $(PO_2)^-$ vibrations in Q^2 groups, generates an FTIR band at around 1265 cm^{-1}[36,42].

A pronounced hydrophobic effect of rubidium ions on the vitreous system was observed. The 1630 cm^{-1} band, assigned to hydroxyl group bending vibrations, decreased progressively in intensity with increasing Rb_2O

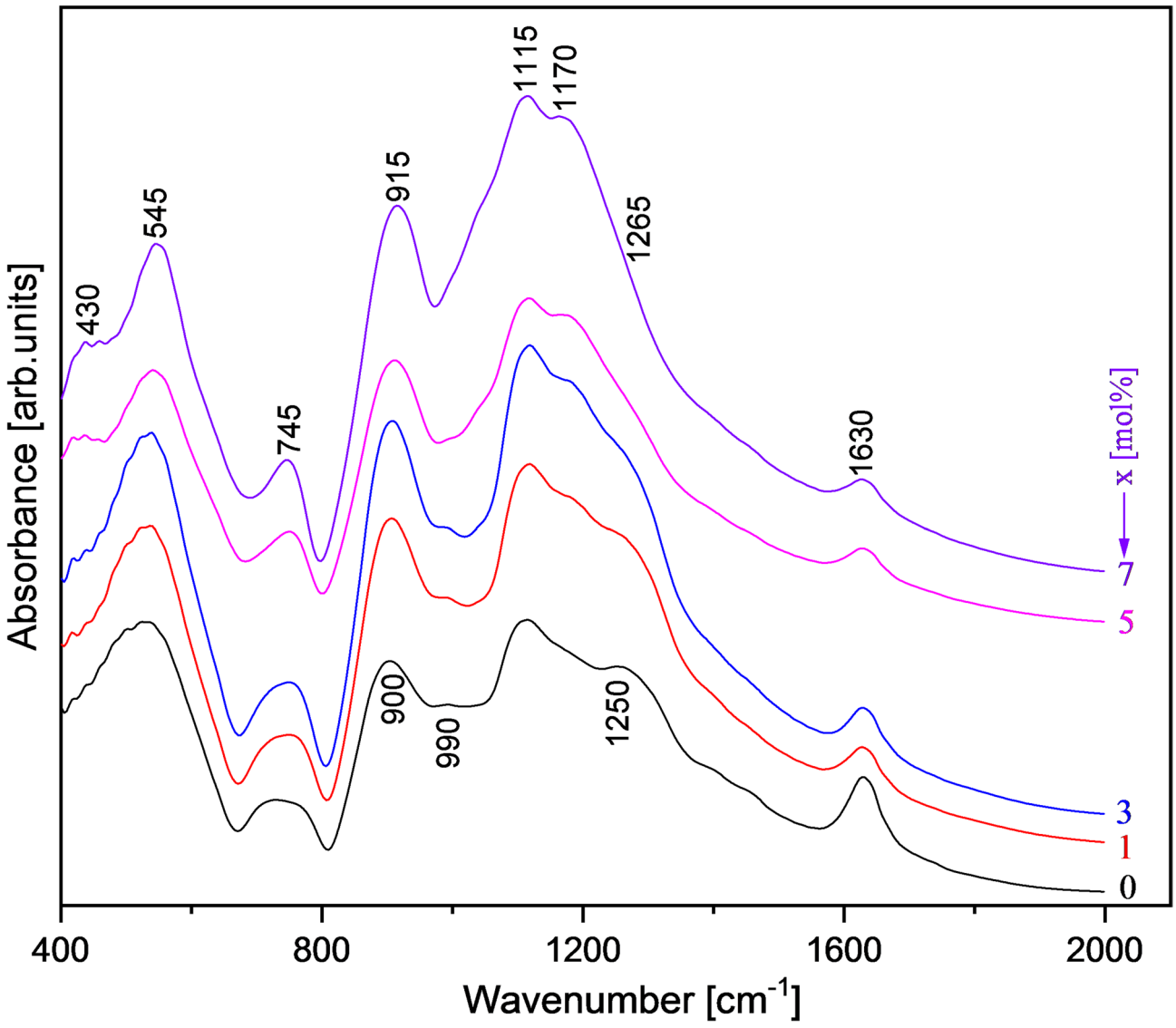

Fig. 2. FTIR spectra of the $xRb_2O·(100-x)[44P_2O_5·25CaO·21Na_2O·5ZnO·5Ag_2O]$ glasses.

content. As phosphate glasses are inherently hydrophilic, this rubidium oxide–induced response highlights a significant enhancement of glass stability over time.

In addition to FTIR spectroscopy, Raman spectroscopy is a powerful tool for elucidating the local structure of glasses, with both techniques providing complementary insights. It is well established that a strong band in the Raman spectrum of a given compound typically corresponds to a weak band in its FTIR spectrum, and vice versa[35]. This complementary relationship arises due to the differing selection rules governing vibrational transitions in these spectroscopic methods. While FTIR spectroscopy primarily detects dipole moment changes associated with vibrational modes, Raman spectroscopy is sensitive to polarizability variations within molecular bonds. Thus, the combined use of FTIR and Raman spectroscopic techniques enables a more comprehensive characterization of glass structure, facilitating a deeper understanding of network connectivity, bond environments, and structural transformations.

The Raman spectra, illustrated in Fig. 3, clearly indicate the structural modifications in the local glass network induced by the addition of rubidium oxide.

The Raman peak from 352 cm^{-1} is due to the bending vibration of PO_4 units[43]. The bending vibration involving different ions (Ca, Na or Rb) and $(P_2O_7)^{4-}$ units (Q^1 tetrahedra) are confirmed by the presence of the absorption peak centred at 531 cm^{-1}. Also, the shoulder from 624 cm^{-1} which increases in intensity with rubidium oxide content can be due to the presence of O-P-O symmetric stretching vibrations[39,43,44].

The Raman spectra reveal a strong band in the range of 701 cm^{-1} to 752 cm^{-1}, which exhibits a decrease in intensity and a shift toward higher wavenumbers with increasing rubidium ion content. The band observed at 701 cm^{-1} corresponds to the stretching vibrations of P–O–P linkages in Q^2 units, while the band at 752 cm^{-1} is attributed to the symmetric P–O–P stretching vibrations of bridging oxygen atoms in Q^1 units[43]. This shift indicates a reduction in the interconnectivity of the phosphate network, as the glass structure transitions from

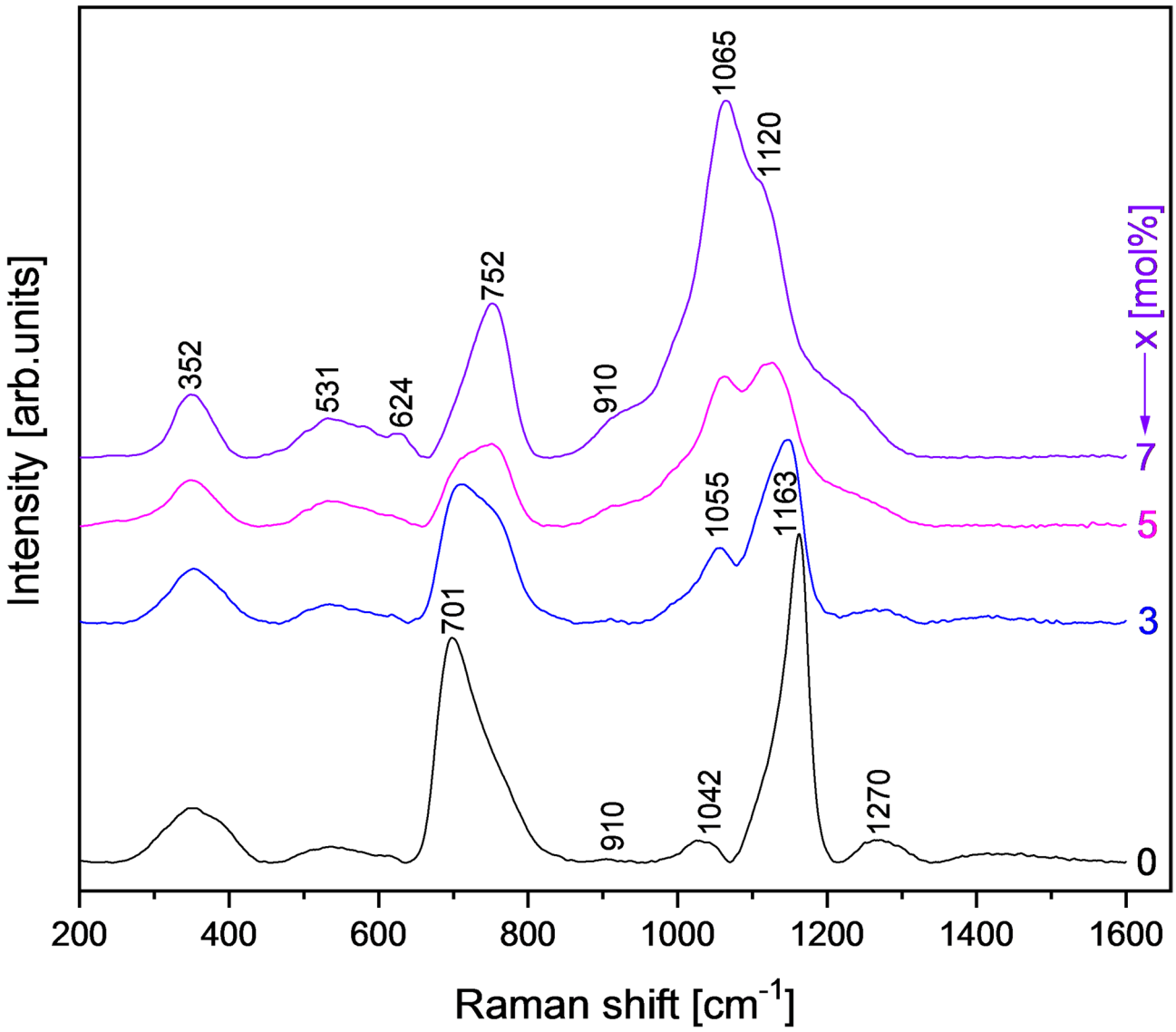

Fig. 3. Raman spectra of the $xRb_2O·(100-x)[44P_2O_5·25CaO·21Na_2O·5ZnO·5Ag_2O]$ glasses.

metaphosphate (Q^2) to pyrophosphate (Q^1) units, suggesting a progressive depolymerization of the phosphate framework.

The introduction of rubidium oxide into the phosphate glass network leads to the appearance of a low-intensity band at approximately 910 cm^{-1}, indicating the formation of orthophosphate units $(PO_4)^{2-}$ (Q^0 tetrahedra) due to the disruption of existing phosphate linkages[38,45]. This indicates a progressive depolymerization of the phosphate structure.

Additionally, the incorporation of rubidium ions into the $44P_2O_5·25CaO·21Na_2O·5ZnO·5Ag_2O$ glass matrix results in an increased intensity of the band centered at 1042 cm^{-1}, which shifts towards 1065 cm^{-1}, also. This shift is associated with the enhanced presence of Q^1 pyrophosphate groups, corresponding to $(P_2O_7)^{4-}$ dimeric units in samples with higher rubidium content[38,44,45]. These structural transformations indicate a reduction in phosphate network connectivity, further supporting the role of rubidium as a network modifier[38,44,45].

A dominant band is observed at 1163 cm^{-1} in the Raman spectra of the glass matrix, corresponding to the symmetric stretching vibrations of PO_2 groups, where two non-bridging oxygens are bound to a phosphorus atom within Q^2 units[44,45]. As the rubidium oxide concentration increases, the intensity of this band decreases, and it shifts towards 1120 cm^{-1}, further confirming the progressive depolymerization of the phosphate network upon Rb_2O addition.

The band centered at 1270 cm^{-1} is attributed to the asymmetric stretching vibrations of PO_2 groups in metaphosphate (Q^2) units[39,44]. A slight decrease in the intensity of this band suggests structural reorganization within the glass network as the rubidium content increases.

Both FTIR and Raman spectroscopic analyses provide strong evidence of phosphate network depolymerization induced by Rb_2O incorporation in the $44P_2O_5·25CaO·21Na_2O·5ZnO·5Ag_2O$ glass matrix. This process is characterized by the progressive transformation of Q^2 metaphosphate units into Q^1 pyrophosphate units.

Notably, starting at 5 mol% Rb_2O, Raman spectroscopy distinctly highlights the network-modifying role of rubidium ions, emphasizing their impact on the glass structure. This structural transformation is expected to influence the physicochemical and biological properties of the bioglasses, further supporting the role of Rb_2O as a key network modifier.

XPS data

Figure 4 presents the XPS survey spectra of the synthesized glass samples, providing insights into their surface composition. The survey spectra were analyzed in terms of peak intensities and positions, allowing for the identification and quantification of all constituent elements within the studied glasses. The corresponding XPS and Auger peaks were clearly distinguished and labeled within the spectra.

The elemental surface compositions of the glass samples, determined from XPS analysis, are presented in Table 1. Rubidium concentrations increased systematically with the nominal Rb_2O content, confirming its successful incorporation into the glass network. In the composition containing 7 mol% Rb_2O, the surface enrichment of rubidium was accompanied by a marked reduction in silver concentration (3.23 at%), indicating a redistribution of surface species. These results demonstrate that rubidium plays a critical role in modulating the surface chemistry of phosphate-based glasses, with direct implications for their biological performance, as detailed in sections "Cell compatibility"–"Antibacterial and antifungal assay".

The high-resolution XPS spectra of Ag 3d provide valuable insights into the silver species present in the glass samples. The deconvoluted Ag 3d photoelectron signals for three representative samples are illustrated in Fig. 5. The spectra confirm the presence of both metallic silver (Ag^0) and ionic silver (Ag^+) at the surface of the glass.

Using Gaussian–Lorentzian (GL30) peak fitting with a Shirley background, the Ag 3d spectra were deconvoluted into two distinct doublets: one located at lower binding energy (green line), corresponding to

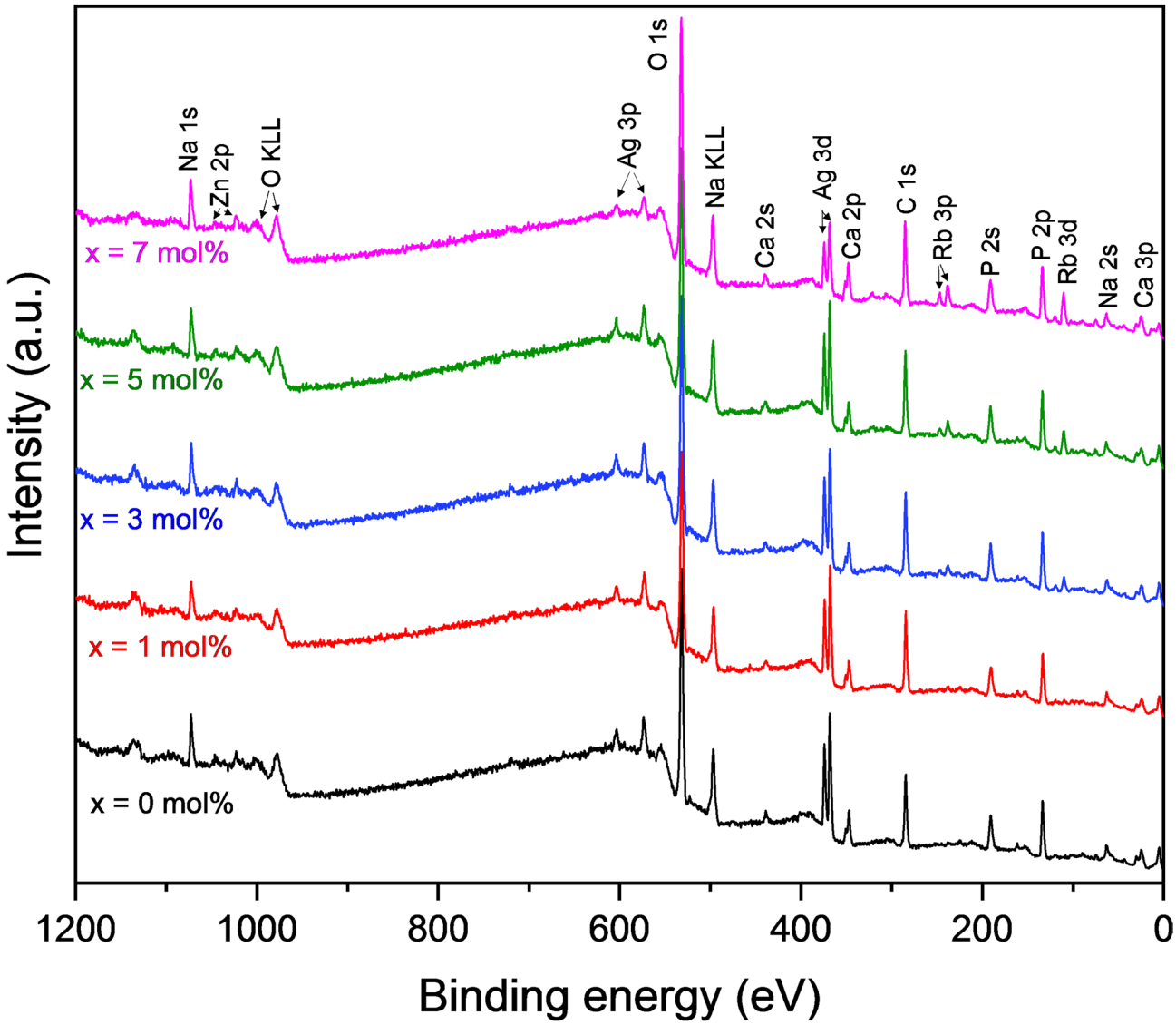

Fig. 4. XPS survey spectra of the $xRb_2O·(100-x)[44P_2O_5·25CaO·21Na_2O·5ZnO·5Ag_2O]$ glasses.

x [mol%]	Elemental concentration (at%)						
	Rb	*P*	Ca	Na	O	Zn	Ag
0	-	30.03	5.47	2.58	54.65	0.92	6.35
1	1.30	32.28	5,30	2.36	51.20	1,08	6.48
3	2.34	30.38	4,79	2.50	52.90	1.06	5.03
5	3.01	30.30	4,68	2.75	52.56	1,01	5.69
7	4.02	30.14	6.15	2.28	53.31	0.87	3.23

Table 1. The elemental composition determined from XPS analysis with an accuracy of ± 0.2 at %.

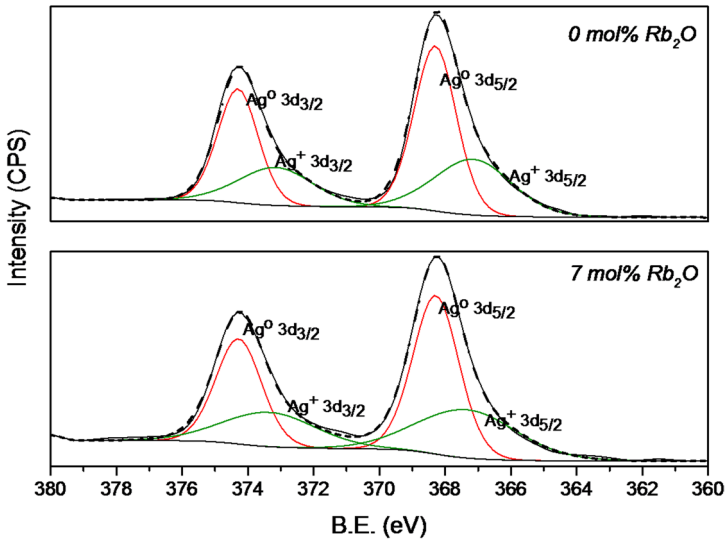

Fig. 5. The high-resolution Ag3d spectrum of samples with x = 0 and 7 mol% Rb_2O. Red line indicates the Ag^0 component and green line the Ag^+ component; dash-dot lines are the fit result.

Ag^+, and the other at higher binding energy (red line), characteristic of Ag^0. These findings indicate that silver exists in both oxidation states across all samples, which is particularly relevant to their antibacterial properties, as further discussed in section "Antibacterial and antifungal assay".

The silver species ratio (Ag^+/Ag^0) was determined from the high-resolution XPS spectra of Ag3d by calculating the area under the corresponding spectral components ($Ag3d_{5/2}$ and $Ag3d_{3/2}$). The results indicate that this ratio remains nearly constant across all samples, with only a slight variation from 0.62 in the base glass matrix to 0.65 in the sample containing 7 mol% Rb_2O. This consistency suggests the successful incorporation of silver into the glass structure and its stable distribution in both metallic (Ag^0) and ionic (Ag^+) states at the surface.

In general, chemical shifts in XPS spectra are highly sensitive to variations in atomic coordination and local structural environments. Figure 6 presents the high-resolution XPS spectra of Rb3d, providing insights into the electronic state and local environment of rubidium in the glass matrix. A noticeable shift toward higher binding energies was observed with increasing Rb_2O content, indicating an increase in the oxidation state. The broad aspect of the Rb3d peaks, along with a slight decrease (approximately 3 eV) in the full width at half maximum (FWHM) as Rb_2O content increases, further suggests a continuous modification in the coordination and bonding environment of rubidium atoms. This behavior is indicative of a progressive change in the number and type of chemical bonds formed by rubidium within the phosphate-based glasses.

TEM images

Figure 7 presents the TEM mapping of two representative glass samples, providing insights into the distribution and morphology of silver nanoparticles (AgNPs) as a function of rubidium oxide content. In the absence of Rb_2O, the silver nanoparticles appear as small, isolated structures with an average size of approximately 50 nm. However, with increasing Rb_2O content, the colloidal AgNPs exhibit significant growth, reaching sizes in the range of 250–500 nm.

Cell compatibility

The success of an implant is preliminary decided by the interaction and response between cells and biomaterial surface. Inadequately adherent cells inhibit tissue repair and regeneration, resulting in implant failure. To assess the cell compatibility of rubidium oxide containing BGs, normal epithelial cells (CCD1137Sk) were selected. All the results obtained are shown in Fig. 8. Overall, the glass matrix demonstrates excellent biocompatibility, highlighting the potential of this composition as a biomaterial.

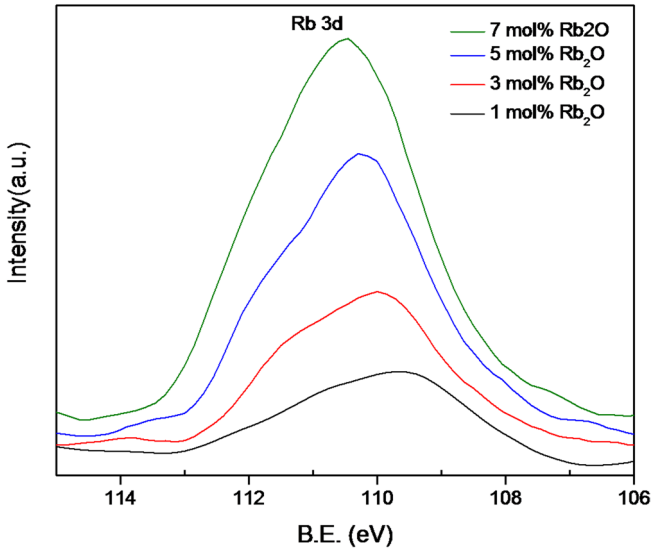

Fig. 6. Rb3d spectra of the $xRb_2O{\cdot}(100\text{-}x)[44P_2O_5{\cdot}25CaO{\cdot}21Na_2O{\cdot}5ZnO{\cdot}5Ag_2O]$ glasses.

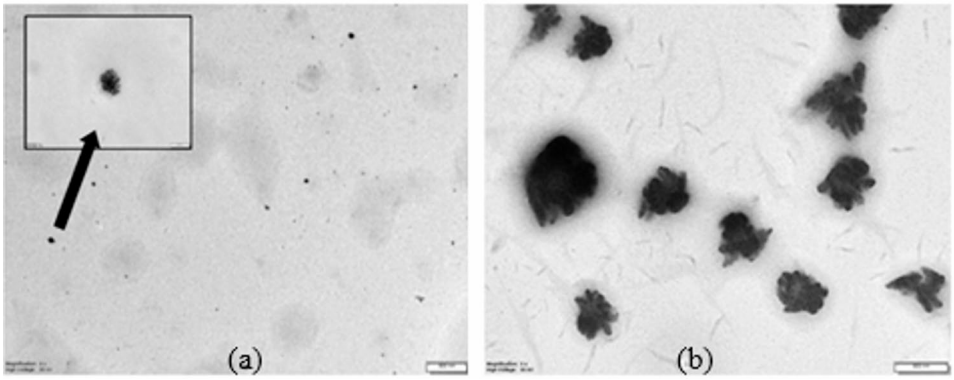

Fig. 7. TEM micrographs of glass matrix (a) and sample containing 5 mol% Rb_2O (b).

Incorporating rubidium oxide (Rb_2O) into the glass matrix composition reduces cellular viability, although the samples remain biocompatible. For the sample containing 3 mol% Rb_2O, a consistent increase in cell viability was observed from 24 to 48 h across all dilutions tested. However, for the sample with 5 mol% Rb_2O, this positive effect was only evident at a concentration of 1.56 µg/mL. In contrast, the sample with 7 mol% Rb_2O remained biocompatible but exhibited a decrease in cell viability from 24 to 48 h across all dilutions. The XPS elemental analysis (Table 1) revealed that at 7 mol% Rb_2O, the surface fraction of rubidium ions reached its highest value (4.02 at%), while the fraction of silver ions was at its lowest (3.23 at%). This finding suggests that rubidium ions play a key role in the reduced proliferation of normal epithelial cells.

Cancer cells killing ability

The anticancer potential of the samples was evaluated using the HS578T breast cancer cell line, with the results summarized in Fig. 9. For the sample without rubidium ions, a modest cytotoxic effect was observed only at a concentration of 3.125 µg/mL after 48 h. However, when the rubidium oxide content exceeded 3 mol%, cell viability decreased below 80% relative to the control. Notably, the sample containing 7 mol% Rb_2O exhibited the most significant cytotoxic effect at a concentration of 0.78 µg/mL after 48 h, reducing cell viability to 75% relative to the control. These findings strongly suggest that rubidium ions are primarily responsible for the observed anticancer activity. The mechanism through which metallic ions exert cytotoxic effects on cancerous cells involves multiple biochemical pathways, with specific impacts varying according to the properties of the metal ion involved. These ions can effectively suppress tumor growth through a combination of mechanisms, including activation of biocatalytic reactions at the tumor site, altering cellular osmolarity, disrupting metabolic processes, interfering with signal transduction pathways, and actively targeting intracellular DNA[46]. The role of rubidium ions (Rb^+) in anticancer activity, while less explored, is thought to share similarities with potassium ions (K^+). Both ions can easily pass through the cell membrane via potassium channels due to their comparable ionic radii, allowing them to affect intracellular ionic balance and membrane potential. Such disruptions can impair

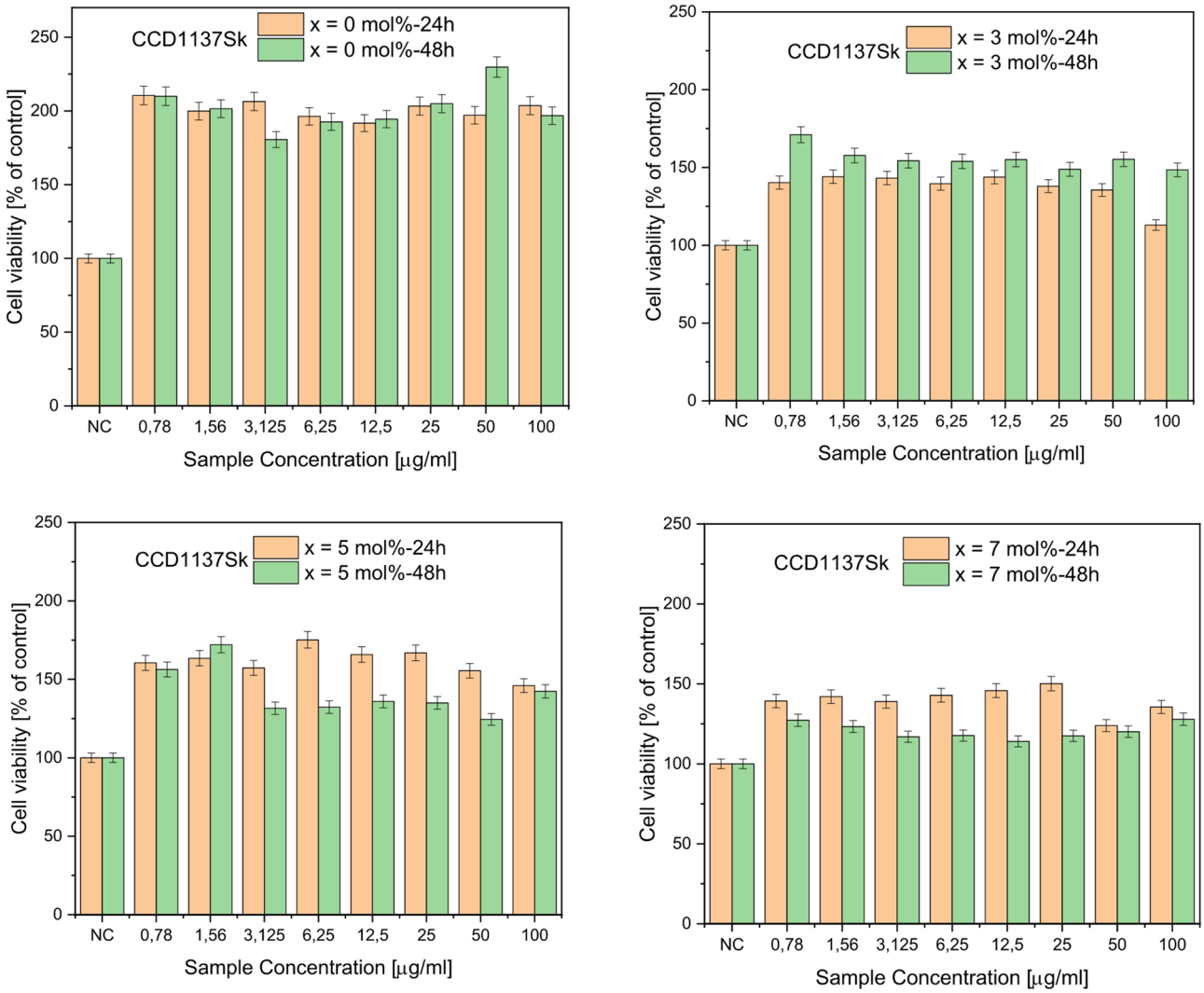

Fig. 8 V. iability of CCD1137Sk cells after 24 and 48 h interaction with different concentration of $xRb_2O·(100-x)[44P_2O_5·25CaO·21Na_2O·5ZnO·5Ag_2O]$ glasses (with NC as negative control and bars as standard error of means).

vital cellular functions, including signaling and volume regulation, potentially triggering apoptosis in cancer cells. Further research is needed to fully elucidate the specific pathways through which Rb^+ ions contribute to anticancer activity and to determine how it might synergize with other therapeutic agents.

Antibacterial and antifungal assay

All the samples studied were tested on *E. coli* (ATCC25922) and *S. aureus* (ATCC 1109R) bacterial lines and *Candida albicans* as fungal line.

All samples had shown a powerful antibacterial effect on the gram-negative *E. coli* even after 1 h. This result strongly indicated the ability of silver ions (Ag^+) found on the glasses surface (XPS results) to penetrate the bacteria's thin wall and kill it.

For *S. aureus* all the samples studied don't present a clear bactericidal effect reported at control sample (Fig. 10). The most notable bacteriostatic effect was observed for the samples 0–3 mol% Rb_2O at 1 and 2 h. This behavior was expected since the gram-positive bacteria are less susceptible to Ag^+ than gram-negative bacteria mainly due to the peptidoglycan particularities[47].

Antifungal possible effect of analyzed BGs was tested on *Candida albicans*, the results being presented in Fig. 11. The investigated samples do not manifest a notable effect on the *Candida albicans*, but we asses that matrix and the sample with 7 mol% Rb_2O are not an appropriate medium for the fungi massive propagation.

Conclusions

Homogeneous glasses of the system $xRb_2O·(100–x)[44P_2O_5·25CaO·21Na_2O·5ZnO·5Ag_2O]$ ($0 \le x \le 7$ mol%) were successfully synthesized by the melt-quenching method. X-ray diffraction confirmed the vitreous state of all compositions, which is noteworthy given the known tendency of silver oxide to segregate into metallic phases

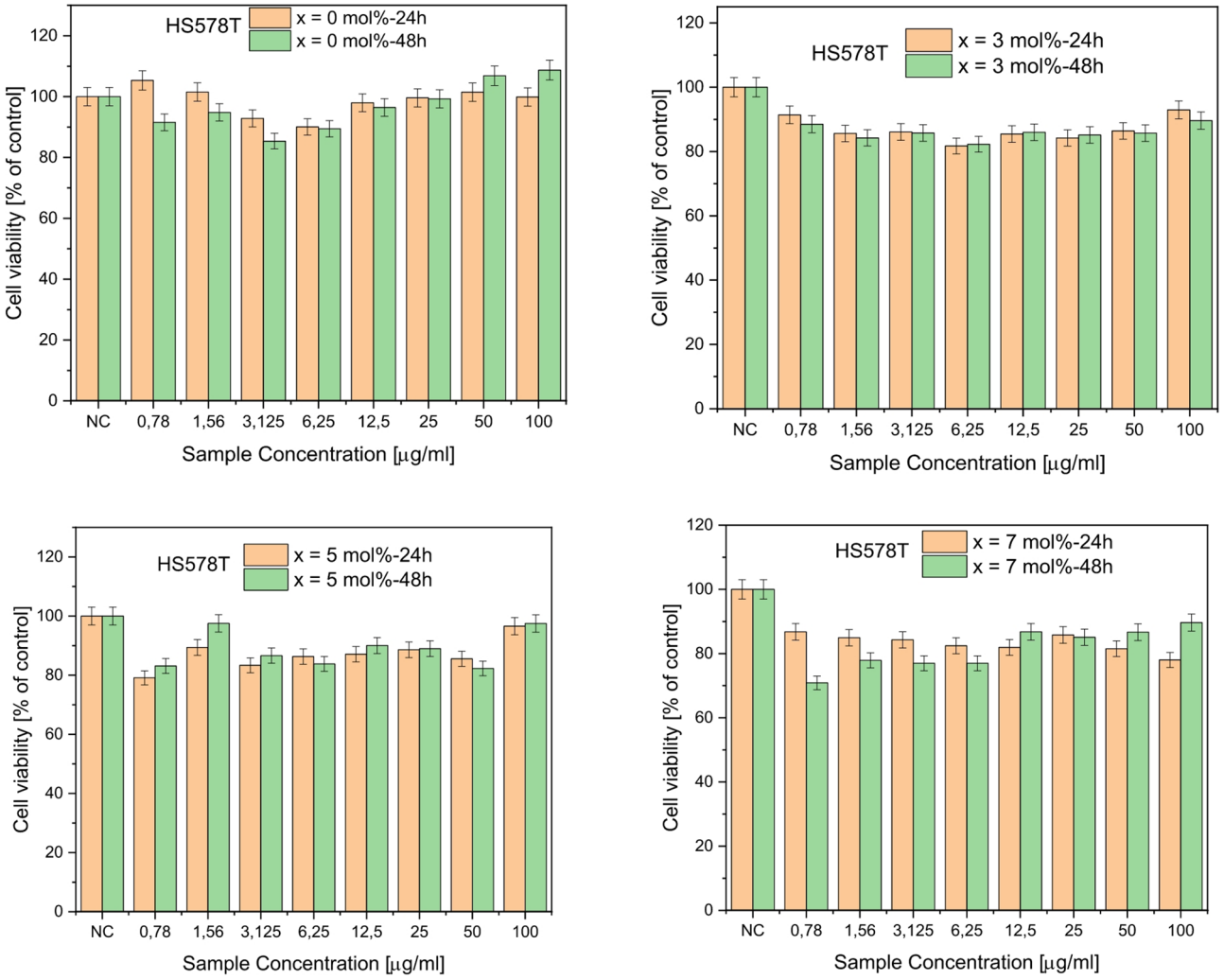

Fig. 9. Viability of HS578T cells after 24 and 48 h interaction with different concentration of $xRb_2O\cdot(100\text{-}x)[44P_2O_5\cdot25CaO\cdot21Na_2O\cdot5ZnO\cdot5Ag_2O]$ glasses (with NC as control and bars as standard error of means).

during quenching. FTIR and Raman spectroscopy demonstrated that progressive incorporation of Rb_2O induces significant modifications in the short-range network structure, with Rb^+ ions acting as network modifiers and promoting phosphate depolymerization through a $Q^2 \rightarrow Q^1$ transition.

Surface analysis by XPS revealed the presence of all constituent elements, with silver detected in both ionic and metallic forms. The highest Ag^+/Ag^0 ratio (0.65) was recorded in the 7 mol% Rb_2O sample, where the overall silver content was lowest (3.23 at%).

Biological assays demonstrated strong antimicrobial efficacy, with all glasses eliminating gram-negative *E. coli* within 1 h via Ag^+ release. Against gram-positive *S. aureus*, a bacteriostatic effect was observed in the 0–3 mol% Rb_2O samples at early exposure times (1–2 h).

The MTT assays confirmed excellent cytocompatibility with healthy epithelial cells (CCD1137Sk), with only a slight decline in viability at higher Rb_2O contents. Notably, the glass containing 7 mol% Rb_2O exhibited selective anticancer activity against the HS578T breast cancer cell line at 0.87 mg mL^{-1} after 48 h, while maintaining compatibility with healthy cells, and showed modest antifungal activity against *Candida albicans*.

Taken together, these findings highlight the potential of multicomponent phosphate-based bioactive glasses as multifunctional biomaterials with combined antibacterial, antifungal, and anticancer properties. The synergistic contributions of Ag^+ and Rb^+ ions play a central role in these effects. Future in vivo studies are essential to elucidate the underlying mechanisms and to validate their safety and therapeutic potential in clinical applications.

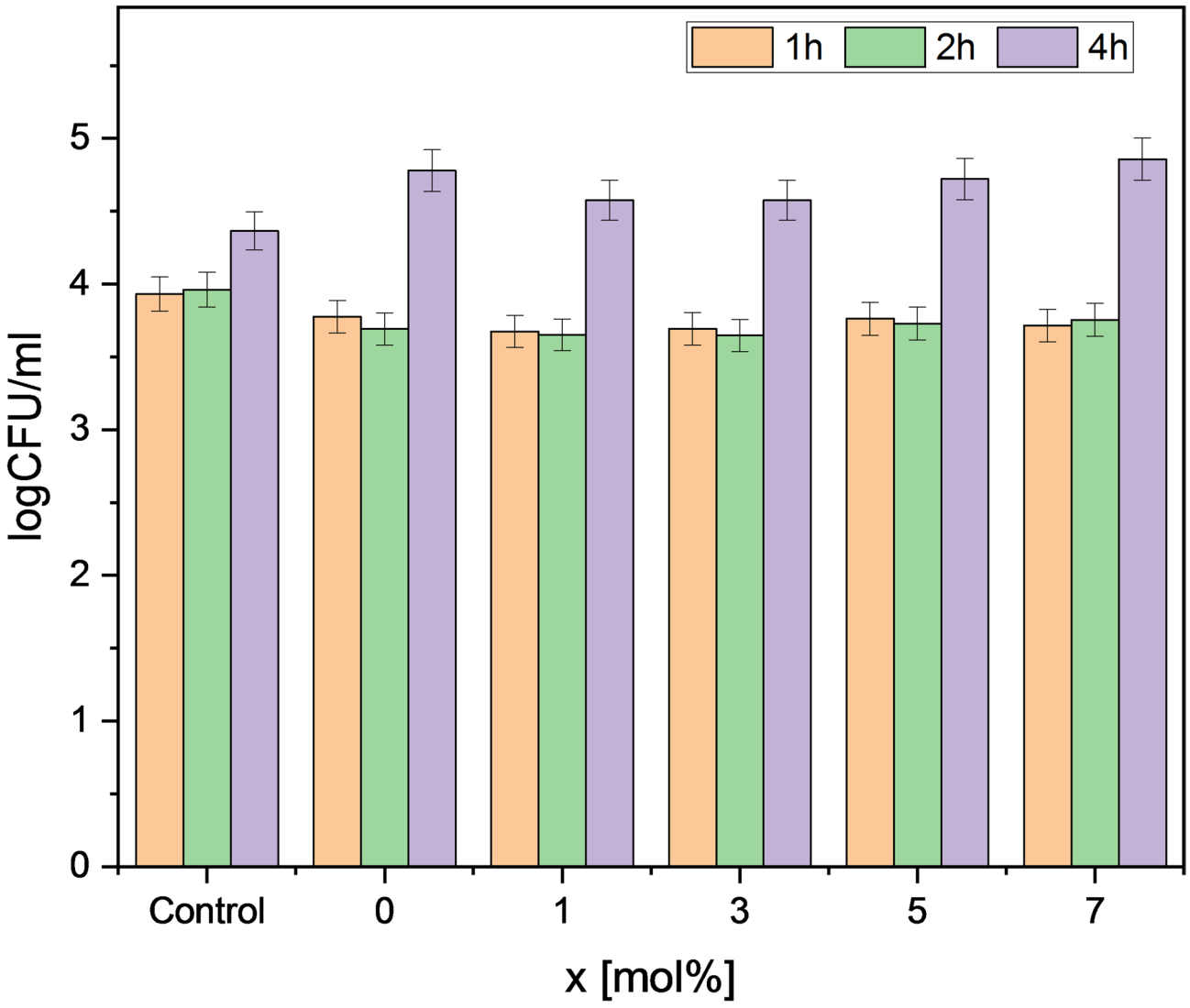

Fig. 10. Antibacterial activity of $xRb_2O\cdot(100\text{-}x)[44P_2O_5\cdot25CaO\cdot21Na_2O\cdot5ZnO\cdot5Ag_2O]$ glasses on *Staphylococcus aureus (*bars indicate standard error of means*)*.

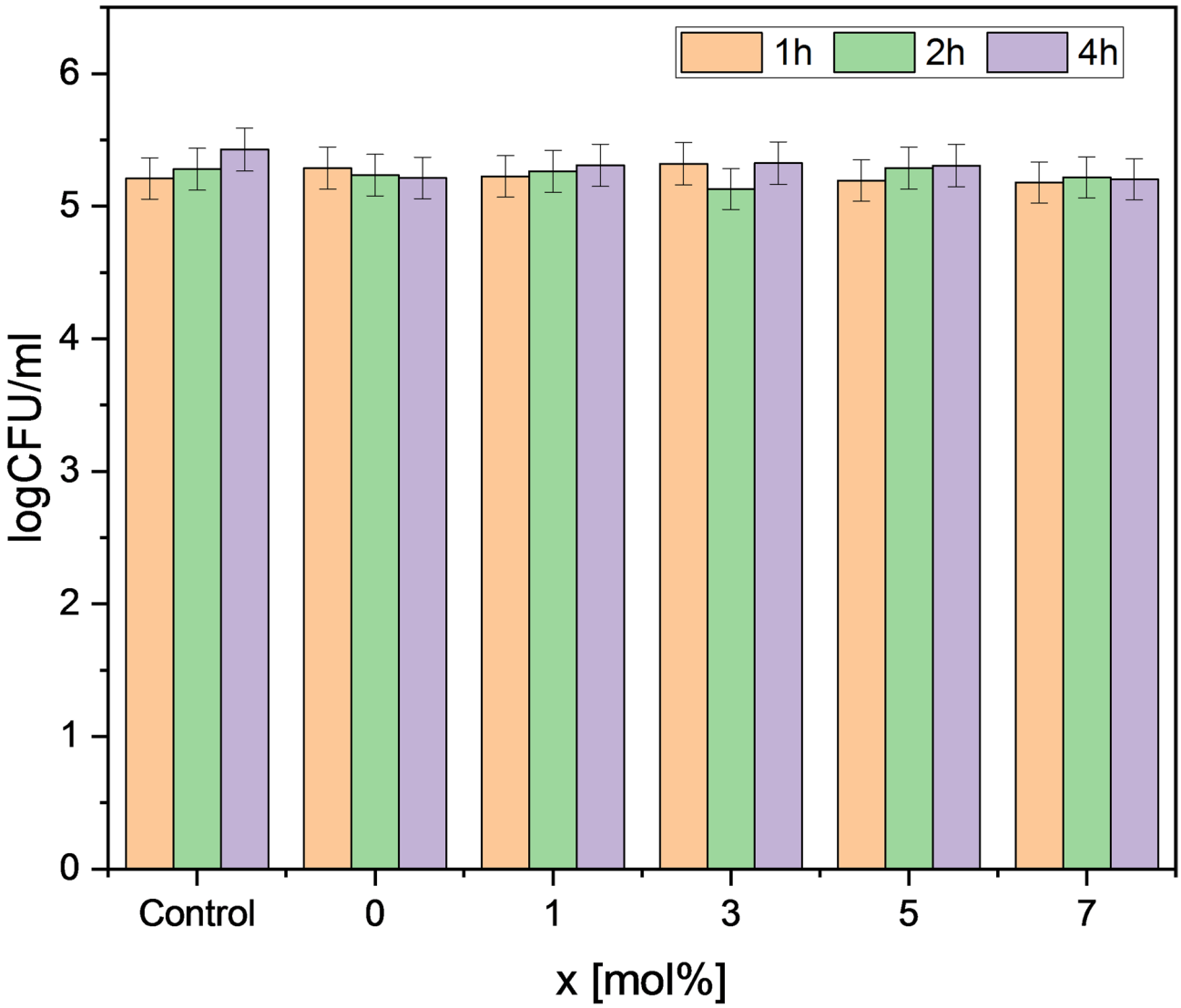

Fig. 11. Antifungal activity of $xRb_2O\cdot(100\text{-}x)[44P_2O_5\cdot25CaO\cdot21Na_2O\cdot5ZnO\cdot5Ag_2O]$ glasses on *Candida albicans* (bars indicate standard error of means).

Data availability

No datasets were generated or analysed during the current study.

Received: 5 April 2025; Accepted: 18 September 2025
Published online: 23 October 2025

References

1. Salih, V. et al. Development of soluble glasses for biomedical use part II: the biological response of human osteoblast cell lines to phosphate-based soluble glasses. *J. Mater. Sci. Mater. Med.* **11**, 615–620. https://doi.org/10.1023/A:1008901612674 (2000).
2. Sharmin, N. & Rudd, C. D. Structure, thermal properties, dissolution behaviour and biomedical applications of phosphate glasses and fibres: a review. *J. Mater. Sci.* **52**, 8733–8760. https://doi.org/10.1007/s10853-017-0784-4 (2017).
3. Kaur, G. et al. Synthesis, cytotoxicity and hydroxyapatite formation in 27-Tris-SBF for sol-gel based $CaO\text{-}P_2O_5\text{-}SiO_2\text{-}B_2O_3\text{-}ZnO$ bioactive glasses. *Sci. Rep.* **4**, 4392. https://doi.org/10.1038/srep04392 (2014).
4. Pandayil, J. T., Boetti, N. G. & Janner, D. Advancements in biomedical applications of calcium phosphate glass and glass-Based Devices-A review. *J. Funct. Biomater.* **15** (1–26). https://doi.org/10.3390/jfb15030079 (2024).
5. Abd El-Hamid, H. K., Farag, M. M., Abdelraof, M. & Elwan, R. L. Regulation of the antibiotic elution profile from tricalcium phosphate bone cement by addition of bioactive glass. *Sci. Rep.* **14**, 2804. https://doi.org/10.1038/s41598-024-53319-2 (2024).
6. Ning, C., Zhou, Z. L. & Tan, G. Fourth-generation biomedical materials. *Mater. Today.* **19**, 2–3. https://doi.org/10.1016/j.mattod.2015.11.005 (2016).
7. Andreu-Perez, J., Leff, D. R., Ip, H. M. D. & Yang, G. Z. From wearable sensors to smart implants—toward pervasive and personalized healthcare. *IEEE Trans. Biomed. Eng.* **62**, 2750–2762. https://doi.org/10.1109/TBME.2015.2422751 (2015).
8. Hoppe, A., Güldal, N. S. & Boccaccini, A. R. A review of the biological response to ionic dissolution products from bioactive glasses and glass-ceramics. *Biomaterials* **32**, 2757–2774. https://doi.org/10.1016/j.biomaterials.2011.01.004 (2011).

9. Pantulap, U., Arango-Ospina, M. & Boccaccini, A. R. Bioactive glasses incorporating less-common ions to improve biological and physical properties. *J. Mater. Sci. Mater. Med.* **33**, 526. https://doi.org/10.1007/s10856-021-06626-3 (2022).
10. Darouiche, R. O. Treatment of infections associated with surgical implants. *N Engl. J. Med.* **350** (14), 1422–1429. https://doi.org/10.1056/NEJMra035415 (2004).
11. Costerton, J. W., Stewart, P. S. & Greenberg, E. P. Bacterial biofilms: a common cause of persistent infections. *Science* **284** (5418), 1318–1322. https://doi.org/10.1126/science.284.5418.1318 (1999).
12. Veerachamy, S., Yarlagadda, T., Manivasagam, G. & Yarlagadda, P. K. Bacterial adherence and biofilm formation on medical implants: a review. *Proc. Institution Mech. Eng. Part. H J. Eng. Med.* **228(10)**, 1083–1099. https://doi.org/10.1177/0954411914556137 (2014).
13. Levin, B. R. & Rozen, D. E. Non-inherited antibiotic resistance. *Nat. Rev. Microbiol.* **4**, 556–562. https://doi.org/10.1038/nrmicro1445 (2006).
14. Molenda, M. & Kolmas, J. The role of zinc in bone tissue health and regeneration-a review. *Rev. Biol. Trace Elem. Res.* **201**, 5640–5651. https://doi.org/10.1007/s12011-023-03631-1 (2023).
15. Yamaguchi, M. Role of zinc in bone formation and bone resorption. *J. Trace Elem. Exp. Med.* **11**, 119–135 (1998).
16. Lee, M. J. et al. Zinc-modified phosphate-based glass micro-filler improves *Candida albicans* resistance of auto-polymerized acrylic resin without altering mechanical performance. *Sci. Rep.* **12**, 19456. https://doi.org/10.1038/s41598-022-24172-y (2022).
17. Tiama, T. M. et al. Molecular and biological activities of metal oxide-modified bioactive glass. *Sci. Rep.* **13**, 10637. https://doi.org/10.1038/s41598-023-37017-z (2023).
18. Ryu, J. H., Kang, T. Y., Choi, S. H., Kwon, J. S. & Hong, M. H. Cerium doping of 45S5 bioactive glass improves redox potential and cellular bioactivity. *Sci. Rep.* **14**, 15837. https://doi.org/10.1038/s41598-024-66417-y (2024).
19. Yukawa, M., Suzuki-Yasumoto, M., Amano, K. & Terai, M. Distribution of trace elements in the human body determined by neutron activation analysis. *Arch. Environ. Heal Int. J.* **35**, 36–44. https://doi.org/10.1080/00039896.1980.10667459 (1980).
20. Yamagata, N. The concentration of common cesium and rubidium in human body. *J. Radiat. Res.* **3** (1), 9–30. https://doi.org/10.1269/jrr.3.9 (1962).
21. Ouyang, S., Zheng, K., Huang, Q., Liu, Y. & Boccaccini, A. R. Synthesis and characterization of rubidium-containing bioactive glass nanoparticles. *Mater. Lett.* **273**, 127920. https://doi.org/10.1016/j.matlet.2020.127920 (2020).
22. Tan, Y., Chen, W., Wei, W., Huang, Q. & He, X. Rubidium-modified bioactive glass-ceramics with hydroxyapatite crystals for bone regeneration. *Trans. Nonferrous Met. Soc. China*. **31**, 521–532. https://doi.org/10.1016/S1003-6326(21)65514-0 (2021).
23. Pantulap, U., Unalan, I. & Zheng, K. Hydroxycarbonate apatite formation, cytotoxicity, and antibacterial properties of rubidium-doped mesoporous bioactive glass nanoparticles. *J. Porous Mater.* **31**, 685–696. https://doi.org/10.1007/s10934-023-01546-9 (2024).
24. He, X. et al. Wound dressings based on rubidium-doped bioactive glass nanospheres promote diabetic wound healing. *J. Biomed. Nanotechnol.* **15**, 2059–2071. https://doi.org/10.1166/jbn.2019.2849 (2019).
25. Alexander, J. W. History of the medical use of silver. *Surg. Infect.* **10** (3), 289–292. https://doi.org/10.1089/sur.2008.9941 (2009).
26. Russell, A. D. & Hugo, W. B. 7 antimicrobial activity and action of silver. *Prog Med. Chem.* **31**, 351–370. https://doi.org/10.1016/S0079-6468(08)70024-9 (1994).
27. Chopra, I. The increasing use of silver-based products as antimicrobial agents: a useful development or a cause for concern? *J. Antimicrob. Chemother.* **59** (4), 587–590. https://doi.org/10.1093/jac/dkm006 (2007).
28. Lemire, J. A., Harrison, J. J. & Turner, R. J. Antimicrobial activity of metals: mechanisms, molecular targets and applications. *Nat. Rev. Microbiol.* **11**, 371–384. https://doi.org/10.1038/nrmicro3028 (2013).
29. Ciobanu, C. S., Iconaru, S. L., Le Coustumer, P., Constantin, L. V. & Predoi, D. Antibacterial activity of silver-doped hydroxyapatite nanoparticles against gram-positive and gram-negative bacteria. *Nanoscale Res. Lett.* **7**, 324. http://www.nanoscalereslett.com/content/7/1/324 (2012).
30. Costescu, A. et al. Fabrication, characterization, and antimicrobial activity, evaluation of low silver concentrations in silver-doped hydroxyapatite nanoparticles. *J. Nanomater.* **2013**, 194854. https://doi.org/10.1155/2013/194854 (2013).
31. Vallet-Regí, M., Salinas, A. J. & Arcos, D. From the bioactive glasses to the star gels. *J. Mater. Sci. Mater. Med.* **17** (11), 1011–1017. https://doi.org/10.1007/s10856-006-0437-7 (2006).
32. Azizabadi, N., Azar, P. A., Tehrani, M. S. & Derakhshi, P. Synthesis and characteristics of gel-derived SiO_2-*CaO*-P_2O_5-SrO-Ag_2O-ZnO bioactive glass: bioactivity, biocompatibility, and antibacterial properties. *J. Non-Cryst Solids*. **556**, 120568. https://doi.org/10.1016/j.jnoncrysol.2020.120568 (2021).
33. Lee, S. H. Silver nanoparticles: synthesis and application for nanomedicine. *Int. J. Mol. Sci.* **17** (4), 865. https://doi.org/10.3390/ijms20040865 (2019).
34. Klug, H. P. & Alexander, L. E. X-ray diffraction procedures for polycrystalline and amorphous materials. *X-Ray Diff. Proc. Polycr. Am. Mater.* **1974**, 992 (1974).
35. Jha, P. K., Pandey, O. P. & Singh, K. FTIR spectral analysis and mechanical properties of sodium phosphate glass–ceramics. *J. Mol. Struct.* **1083**, 278–285. https://doi.org/10.1016/j.molstruc.2014.11.027 (2015).
36. El-Batal, A. M., Saeed, A., Hendawy, N., El-Okr, M. M. & El-Mansy, M. K. Influence of mo or/and Co ions on the structural and optical properties of phosphate zinc lithium glasses. *J. Non-Cryst Solids*. **559**, 120678. https://doi.org/10.1016/j.jnoncrysol.2021.120678 (2021).
37. Zhang, L. Y., Li, H. & Hu, L. L. Statistical structure analysis of GeO_2 modified Yb^{3+}: Phosphate glasses based on Raman and FTIR study. *J. Alloys Compd.* **698**, 103–113. https://doi.org/10.1016/j.jallcom.2016.12.175 (2017).
38. Ciceo-Lucacel, R., Todea, M. & Simon, V. Effect of selenium addition network connectivity in P_2O_5-CaO-MgO-Na_2O glasses. *J. Non-Cryst. Solids* **488**, 10–13. https://doi.org/10.1016/j.jnoncrysol.2018.03.009 (2018).
39. Kiani, A. et al. Structural characterization and physical properties of P_2O_5–CaO–Na_2O–TiO_2 glasses by Fourier transform infrared, Raman and solid-state magic angle spinning nuclear magnetic resonance spectroscopies. *Acta Biomater.* **8**, 333–340. https://doi.org/10.1016/j.actbio.2011.08.025 (2012).
40. Aly Okasha, A. M. & Abdelghany, M. Zinc phosphate glasses embedded cds quantum Dots for LED lightening application. *J. Opt.* **52** (4), 2207–2213. https://doi.org/10.1007/s12596-023-01280-0 (2023).
41. Ahmed, H., Hammad, A. M. & Abdelghany Optical and structural investigations of zinc phosphate glasses containing vanadium ions. *J. Non-Cryst Solids* **433**, 14–19. https://doi.org/10.1016/j.jnoncrysol.2015.11.016 (2016).
42. Abdelghany, A. M. et al. Structural and gamma-ray Attenuation of mixed former lead-free borophosphate glasses. *Radiat. Phys. Chem.* **214**, 111276. https://doi.org/10.1016/j.radphyschem.2023.111276 (2024).
43. Kuczek, J. et al. Raman and Mossbauer studies of iron phosphate-silicate glasses. *J. Mol. Struct.* **1170**, 82–89. https://doi.org/10.1016/j.molstruc.2018.05.034 (2018).
44. Carta, D. et al. A structural study of sol-gel and melt-quenched phosphate-based glasses. *J. Non-Cryst Solids*. **353** (18–21), 1759–1765. https://doi.org/10.1016/j.jnoncrysol.2007.02.008 (2007).
45. Möncke, D. & Eckert, H. Review on the structural analysis of fluoride-phosphate and fluoro-phosphate glasses. *J. Non-Cryst Solids: X*. **3**, 100026. https://doi.org/10.1016/j.nocx.2019.100026 (2019).
46. Liu, Y., Wang, Y., Song, S. & Zhang, H. Cancer therapeutic strategies based on metal ions. *Chem. Sci.* **12**, 12234. https://doi.org/10.1039/d1sc03516a (2021).
47. Kawahara, K., Tsuruda, K., Morishita, M. & Uchida, M. Antibacterial effect of silver zeolite on oral bacteria under anaerobic conditions. *Dent. Mater.* **16** (6), 452–455. https://doi.org/10.1016/s0109-5641(00)00050-6 (2000).

Author contributions

M.B. contributed to samples preparation, investigation and reviewing and editing of the manuscript; L.B. contributed to samples preparation, investigation, writing of the original draft, reviewing and editing of the manuscript; L.P. contributed to samples preparation, investigation, writing of the original draft; R. L.-C. contributed to conceptualization, methodology, supervision, investigation, writing of the original draft, reviewing and editing of the manuscript; G.S., R.F.B., I.L., O.R.K., A.O., D.C., A.B.T,, G.K. and D.S. contributed to investigation; P.P. contributed to conceptualization, methodology, supervision, samples preparation, investigation, writing of the original draft, reviewing and editing of the manuscript.

Competing interests

The authors declare no competing interests.

Additional information

Correspondence and requests for materials should be addressed to R.L.-C. or P.P.

Reprints and permissions information is available at www.nature.com/reprints.

Publisher's note Springer Nature remains neutral with regard to jurisdictional claims in published maps and institutional affiliations.